Available online at www.sciencedirect.com

SciVerse ScienceDirect

Journal of the European Ceramic Society 32 (2012) 1711–1723

www.elsevier.com/locate/jeurceramsoc

A novel approach to sintering (Ba,Ca)(Ti,Zr)O_3 multilayer ceramic capacitors with Ni electrodes

Shih-Hao Wang[a], Yin-Lai Chai[b], Wen-Hsi Lee[a,*]

[a] Department of Electrical Engineering, National Cheng Kung University, Taiwan, ROC
[b] Department of Jewelry Technology, The Dahan Institute of Technology, Taiwan, ROC

Received 25 May 2011; received in revised form 29 November 2011; accepted 11 December 2011
Available online 22 February 2012

Abstract

In this study, a novel sintering technique combining rapid heating and constrained sintering was adopted to fire multilayer ceramic capacitors (MLCCs). It was demonstrated that chamber development can be significantly minimized, leading to a small internal residual stress in MLCCs when they were fired by the novel sintering technique instead of free sintering. The magnitude of tensile stress was closely related to the heating rate and the thickness of the constraining layer. The presence of in-plane tensile stress resulted from the constrained sintering in the x–y plane of the MLCCs, which then modified both the densification rate of the dielectric materials and the inner electrode. The thin inner electrode (<1 μm) with high continuity (>98%) and the fine grain size (1.5 μm) with narrow distribution (±0.10 μm) of BCTZ-based MLCC with a concave-free morphology can be attained by using such a rapid constrained sintering technique when BT is used as a constraining layer laminated on both sides of the multilayer BCTZ-based MLCC.

Keywords: Sintering; Grain size; Dielectric properties; $BaTiO_3$; Capacitors

1. Introduction

Determining how to obtain the homogeneous microstructure of a multilayer ceramic device is challenging, particularly for a multilayer ceramic capacitor, because $BaTiO_3$-based MLCCs are typically composed of up to five additives. Furthermore, the concentration of each dopant is often less than 1 mol%, with the remaining 90–95 mol% being $BaTiO_3$, and conventional mixing of the metal oxide powder is typically used to prepare $BaTiO_3$-based MLCCs. Thus, it is very difficult to obtain the homogeneous microstructure of $BaTiO_3$-based MLCCs by dispersing the slurry well. However, this problem can be solved when a multilayer ceramic device is fired by hot-pressing. Hot-pressing has been widely applied to the manufacturing of multilayer ceramic substrate, but it has two main disadvantages: one is a longer sintering profile, and the other is the difficulty of mass production of multilayer ceramic devices due to the special design of the hot-pressing sintering furnace.[1] However, during green processing and sintering at a lower temperature, there is no need for the extra pressing of the constraining layers since they are laminated on both sides of the multilayer ceramic device; thus, the shrinkage in the x–y planes of the device is minimized due to the friction force present between the constraining layer and the device.[2,3] The main disadvantage for constrained sintering is the formation of concave morphology at the edge of the multilayer ceramic device, which is attributed to the increase in the shrinkage rate from the interface of the constraining and constrained layers to the middle of the constrained layer.[4,5] This phenomenon is due to the fact that the in-plane tensile stress, which is caused by the constrained sintering and reduced driving force of densification, decreases from the constraining layer interface to the middle of the constrained and constraining layers.

As previously reported, a rapid heating sintering has been used to fire multilayer ceramic capacitors with Ni electrodes.[6] Typically, the evolution of ceramic–ceramic and ceramic–metal constrained multilayers can be described by a viscous flow

---

[*] Corresponding author at: Department of Electrical Engineering, National Cheng Kung University, No. 1 University Road, 701 Taiwan, ROC.
E-mail address: leewen@mail.ncku.edu.tw (W.-H. Lee).

doi:10.1016/j.jeurceramsoc.2011.12.012

model,[7] where elastic stresses are generated because of the mismatch of the densification kinetics of adjacent layers 1 and 2, which can be expressed as follows:

$$\sigma_1 = \left(\frac{1}{1+mn}\right)\eta_1 \Delta\dot{\varepsilon} \tag{1}$$

where m is the layer thickness ratio, n is the viscosity ratio between the layers and $\Delta\dot{\varepsilon}$ is the mismatch of the densification rates. The elastic stress level in MLCCs should be reduced with a faster sintering rate. The heating rate is a powerful processing parameter for controlling the evolution of the grain microstructure. Rapid heating can be used for constrained sintering to allow quick passage through the temperature range where different onset sintering temperatures of Ni film, constrained dielectric and constraining ceramic prevail over their densification.[8]

Based on the above review of various sintering methods, a novel sintering technique combining constrained sintering and rapid heating has been proposed in this study. The objective of the present study was to improve the homogeneity of microstructures and the stability of the inner electrodes of BCTZ-based MLCCs by rapid constrained sintering, with an emphasis on the residual stress of BCTZ-based MLCCs in relation to the sintering conditions. The residual stress was investigated by X-ray diffraction with the aim of elucidating the relationship between residual stress and microstructure, grain size and continuity of Ni electrode of BCZT-based MLCCs.

2. Experiment

2.1. Preparation of MLCCs

$(Ba,Ca)(Ti,Zr)O_3$-based MLCCs were fabricated by conventional multilayer ceramic technology.[9] $BaTiO_3$ (Mitsui, Japan) and dopants, including: $CaCO_3$, ZrO_2, MnO_2, Nb_2O_5, Dy_2O_3 and SiO_2, were weighed, mixed, dispersed and milled in deionized water with 2 mm ZrO_2 beads for 6 h. The mean particle size (D_{50}) of the milled slurry was controlled to be approximately 0.65 μm. Premilling, the slurry was mixed with 7 wt% PVB binder and 1 wt% TEG plasticizer. The resulting slip was cast into a green sheet 4 μm in thickness using a slot-die caster. $Ni/BaTiO_3 = 80/20$ inner paste was printed onto the 80 green sheets, which were then stacked. Two constrained layers (non-reactive borosilicate glass + 98 wt% $BaTiO_3$) with thicknesses of 120, 200 and 280 μm were laminated on both sides of the multilayer $(Ba,Ca)(Ti,Zr)O_3$-based MLCCs. The green sheets were laminated and cut into chips 1.0 mm × 0.5 mm × 0.5 mm. The green chips were debinded at 320 °C for 10 h, and then sintered at 1050–1150 °C for 2 h soaking time at heating rates of 200, 1500 and 3000 °C/H in 95/5 N_2/H_2 wet forming gas. The Cu outer paste was dipped and cured at 900 °C for 10 min in an N_2 atmosphere.

2.2. Measurements

Thermal mechanical analysis (TMA-50, Shimadzu, Japan) was carried out on the green samples to obtain a shrinkage schedule. The microstructures of the specimens were characterized using a scanning electron microscope (Leo 1530, Philips Instrument) equipped with an energy-dispersive spectrometer (EDS; EDAX). Thermal etching was performed at 950 °C for 20 min to reveal the grain boundaries. Grain size was measured by the linear intercept method.

The residual stress was estimated using X-ray diffraction.[10] X-rays were applied to the top surfaces perpendicular to the internal electrodes of the MLCCs. The residual stresses in the length direction were measured. The average residual stress in the MLCCs was calculated through the following formula:

$$\sigma = -\frac{E}{2(1+\gamma)}\cot\,\theta\left(\frac{\pi}{180}\right)\frac{\partial 2\theta}{\partial \sin^2\,\psi} \tag{2}$$

where the elastic module, E, is 250 GPa, as measured by the nanoindentation technique, while Poisson's ratio γ for $(Ba,Ca)(Ti,Zr)O_3$ is 0.25, and the bias angle ψ equals 0, 10, 20 and 40°.

The continuity of the Ni electrode was quantified based on the measurements from optical-microscope images. The average values and standard deviations were calculated based on five images for each MLCC sample.

3. Results and discussion

3.1. Shrinkage rate and chamber development

The constrained sintering technique in this study involved using non-reactive $BaTiO_3$ in the constrained layers. A sandwich structure of $BaTiO_3/(Ba,Ca)(Ti,Zr)O_3$-based MLCC/$BaTiO_3$ was fabricated. The in-plane shrinkage of the $(Ba,Ca)(Ti,Zr)O_3$-based MLCC tape was reduced by using a non-reactive $BaTiO_3$ tape which densified in a different temperature region than the BCTZ-based MLCC tape. The typical shrinkage curves of Ni + BT film, BCTZ tape and BT tape fired at a constant heating rate of 10 °C/min in a reducing atmosphere are shown in Fig. 1, along with the significant sintering mismatch between these three materials. The shrinkage of the Ni film started at approximately 800 °C and stopped at 1000–1100 °C with a total strain of 20%. For the BCTZ and BT tapes, the onset densification temperature was in the range of 1000–1050 °C and 1100–1150 °C, respectively. BCTZ shrinkage rates were almost complete at 1250 °C with a total strain of 17%. As noted, the BCTZ tape began to densify when the shrinkage of Ni was almost finished. We expected that the shrinkage curves for the three materials would shift to a higher temperature as the heating rate increased.

The effect of the thickness of the constraining layer of the BCTZ-based MLCCs on the shape of MLCCs was investigated. The shrinkage of the MLCCs was measured in three directions: length, width and thickness. Fig. 2(a)–(c), respectively, shows the shrinkage in the x direction of the MLCCs in terms of the sintering temperature by free sintering and by constrained sintering at heating rates of 1500 °C/H and 3000 °C/H. Obviously, the densification of the device decreased as the thickness of the constraining layer increased. As Fig. 2(a) shows, the shrinkage rate in the x direction of the MLCCs fired by free sintering

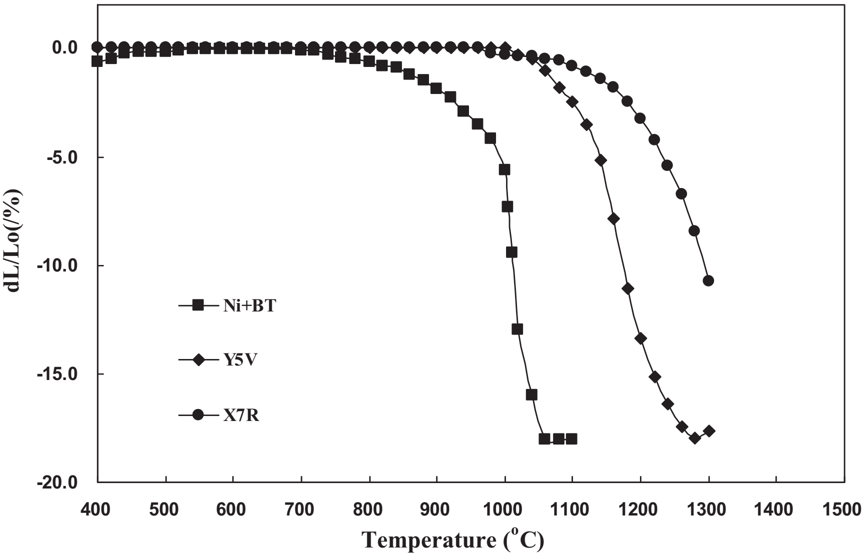

Fig. 1. Shrinkage curves of Ni + BT film, BCTZ tape and BT tape fired at a constant heating rate of 10 °C/min in a reducing atmosphere.

and by constrained sintering achieved a maximum of −15% at 1100 °C and 1150 °C, respectively, at a heating rate of 200 °C/H. These results indicated that the densification temperature would be reduced by approximately 50 °C with constrained sintering instead of free sintering at a low heating rate. Fig. 2(b) and (c) shows the shrinkage rate in the *x* direction of MLCCs fired by free sintering and by constrained sintering at a heating rate of 1500 °C/H and 3000 °C/H, respectively. Clearly, the discrepancy in the densification temperature of MLCCs fired by free and by constrained sintering was shortened when the heating rate was increased, indicating that the friction force generated by constrained sintering decreased as the heating rate increased. The magnitude of fiction force resulted from the mismatches between the constrained layer and the constraining layer during constrained sintering. There were three matches during constrained sintering: the difference of densification onset temperature, densification rate and densification strain between the constrained and the constraining layers.[11] The mismatch of the densification onset temperature could be minimized, accompanied by a reduction in the magnitude of friction force as the heating rate increased.

Fig. 3(a)–(c) shows the shrinkage rate in the *z* direction of MLCCs in terms of the sintering temperature, respectively, by free-sintering and by constrained sintering with heating rates of 200 °C/H, 1500 °C/H and 3000 °C/H. Obviously, the shrinkage rate in the *z* direction in terms of the sintering temperature was completely different from that in the *x* direction. At the high heating rates of 1500 °C/H and 3000 °C/H, there was no significant difference in the shrinkage rate in the *z* direction in terms of the sintering temperature between MLCCs fired by free and by constrained sintering. The shrinkage rate in the *z* direction increased with increase in sintering temperature. However, at a low heating rate of 200 °C/H, the shrinkage rate in the *z* direction increased with the increase in sintering temperature, but the shrinkage rate in the *z* direction of MLCCs fired by constrained sintering was −17%, so it was larger than the −15% by free sintering, especially for MLCCs fired by constrained sintering with a thicker constraining layer of 280 μm. The discrepancy in shrinkage between the *x* direction and the *z* direction can be explained by means of the schematic diagram shown in Fig. 4. The shrinkage of MLCCs fired by free sintering was isotropic, meaning that the shrinkages in the *x*, *y* and *z* directions were identical. However, the shrinkage of MLCCs fired by constrained sintering was non-isotropic. The shrinkage rate in the *x* and *y* directions between the constrained layer and the constraining layer was significantly different, leading to the belief that the shrinkage rate in the *x* and *y* directions was retarded. On the other hand, the shrinkage rate in the *z* direction of MLCCs fired by constrained sintering was almost the same as that by free sintering, i.e., if we did not consider the in-plane friction force generated from the constrained sintering on the shrinkage in the *x* and *y* directions. This fact was due to the thickness of the constraining layer being extremely thin compared to the *x*–*y* area of the constraining layer, so the constrained effect in the *z* direction could be ignored. However, if we considered the in-plane friction force generated from the constrained sintering on the shrinkage in the *x* and *y* directions, the shrinkage rate of the *z* direction would be enhanced by the in-plane friction force; thus leading to the conclusion that the net shrinkage rate in the *z* direction of MLCCs fired by constrained sintering was larger than that for free sintering.

The difference of shrinkage rates in the *x* and *y* directions and the *z* direction was enhanced for MLCCs fired by constrained sintering with a slow heating rate or a thicker constraining layer due to the presence of the significant mismatch between the constrained and the constraining layers during co-firing.

Fig. 5(a)–(c), respectively, shows the morphology at the edge of MLCCs fired by free sintering and by constrained sintering at heating rates of 200 °C/H and 3000 °C/H. The typical concave morphology at the edge of MLCCs fired by constrained sintering with a slow heating rate of 200 °C/H is shown in Fig. 5(a). The concave morphology was attributed to the increase in the

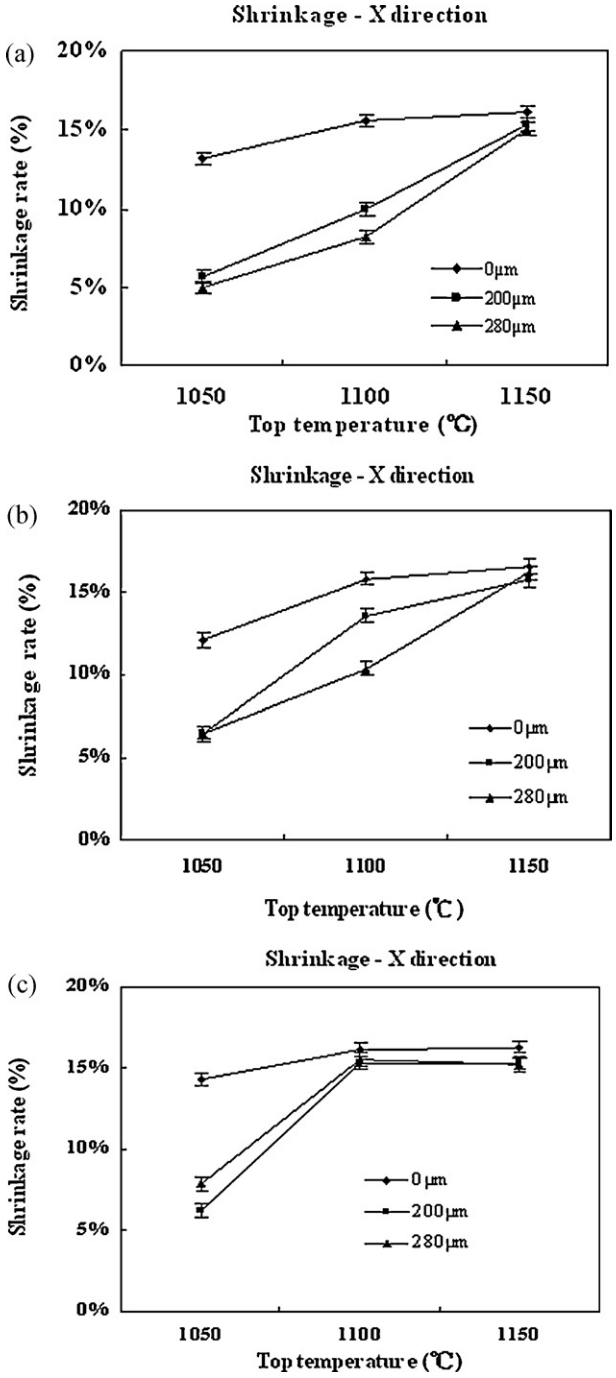

Fig. 2. (a)–(c) Shrinkage in the *x* direction of MLCCs fired, respectively, by free sintering and by constrained sintering with heating rates of 1500 °C/H and 3000 °C/H as a function of sintering temperature.

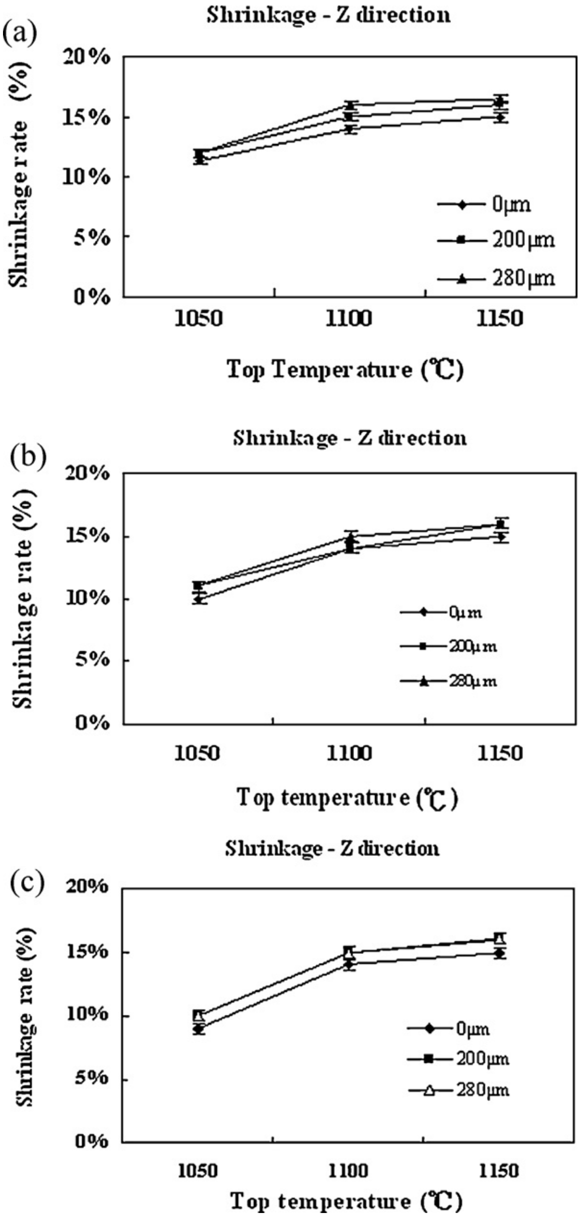

Fig. 3. (a)–(c) Shrinkage in the *z* direction of MLCCs fired, respectively, by free sintering and by constrained sintering with heating rates of 1500 °C/H and 3000 °C/H as a function of sintering temperature.

shrinkage rate from the interface of the constraining and the constrained layers to the middle of the constrained layer. This phenomenon was due to the fact that the in-plane tensile stress, caused by constrained sintering to reduce the driving force of densification, decreased from the interface of the constraining layer and the constrained layer to the middle of the constrained layer. As noted, the morphology at the edge of the MLCCs was straight and concave-free and the same as that by free sintering, as shown in Fig. 5(b) and (c). Although these devices were fired by constrained sintering, the heating rate was much higher than that shown in Fig. 5(a). This discrepancy was associated with a reduction of in-plane tensile stress due to the high heating rate, which in turn led to a small mismatch in the densification onset temperature. In other words, the three kinds of materials: Ni film, BCTZ constrained dielectric and BT constraining layer, shrunk almost simultaneously. We expected that the difference in the densification onset temperature between the constraining layer and constrained layer could be ignored when the MLCCs were fired by constrained sintering with a high heating rate.

The resulting concave-free morphology of MLCCs fired by constrained sintering with a high heating rate agreed with the results for the shrinkage rate in the *x* direction, as shown in Fig. 2. Although the constraining layer could significantly suppress

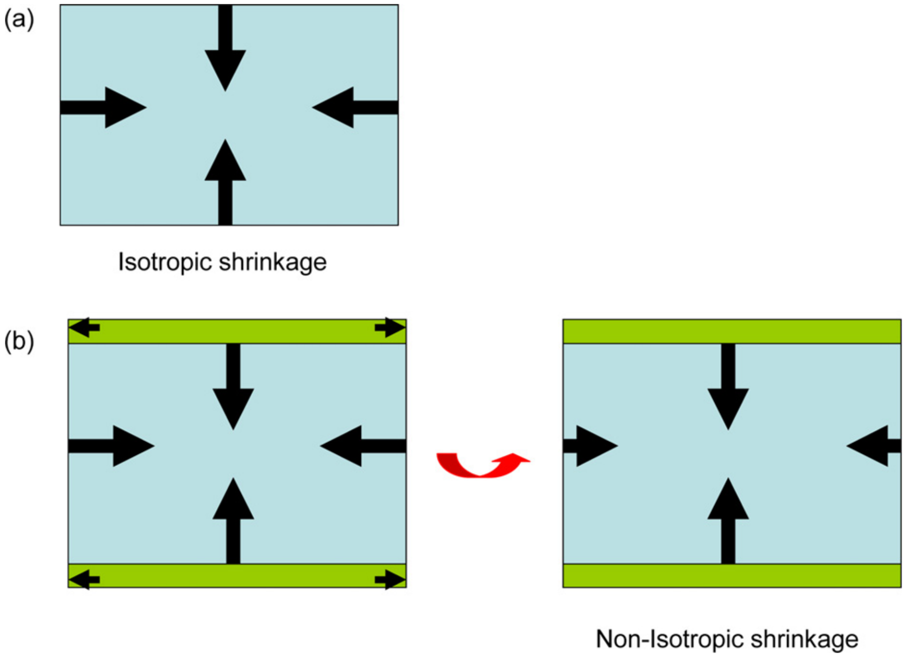

Fig. 4. (a) and (b) Schematic diagram of the isotopic shrinkage of MLCCs fired by free sintering and the non-isotropic shrinkage of MLCCs fired by constrained sintering.

the driving force of densification of the constrained dielectric during constrained sintering, a significant reduction in the in-plane tensile stress was achieved by eliminating the difference in the densification onset temperature during constrained sintering through a high heating rate.

3.2. Residual stress measurement

It was supposed that the mismatched sintering kinetics of the three materials: Ni electrode, the constrained BCTZ dielectric and the constraining layer, led to the development of the in-plane

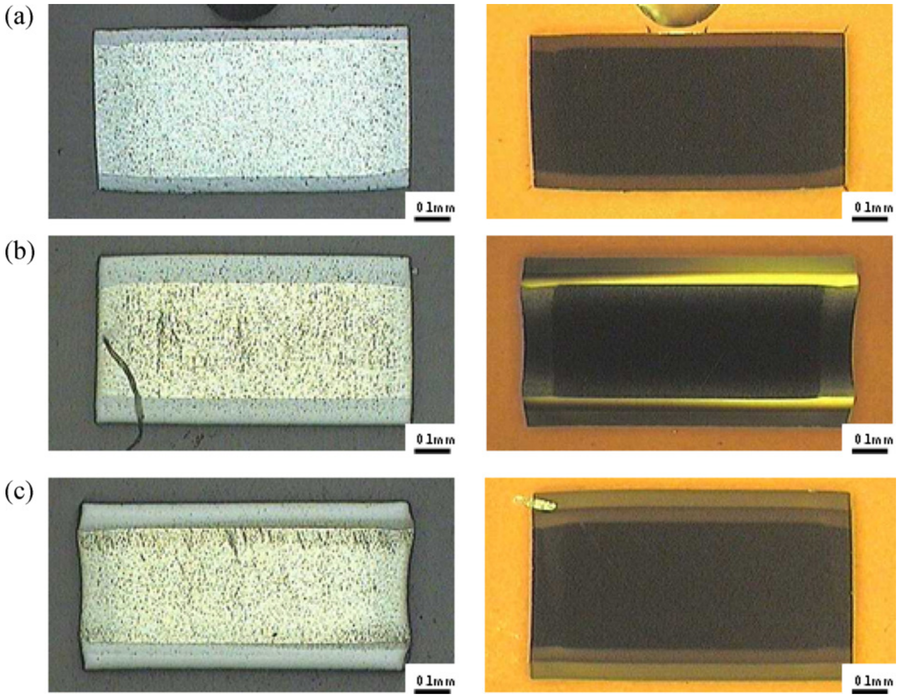

Fig. 5. (a)–(c) Morphology at the edge of MLCCs fired, respectively, by free sintering and by constrained sintering with a slow heating rate (200 °C/H) and a high heating rate (3000 °C/H).

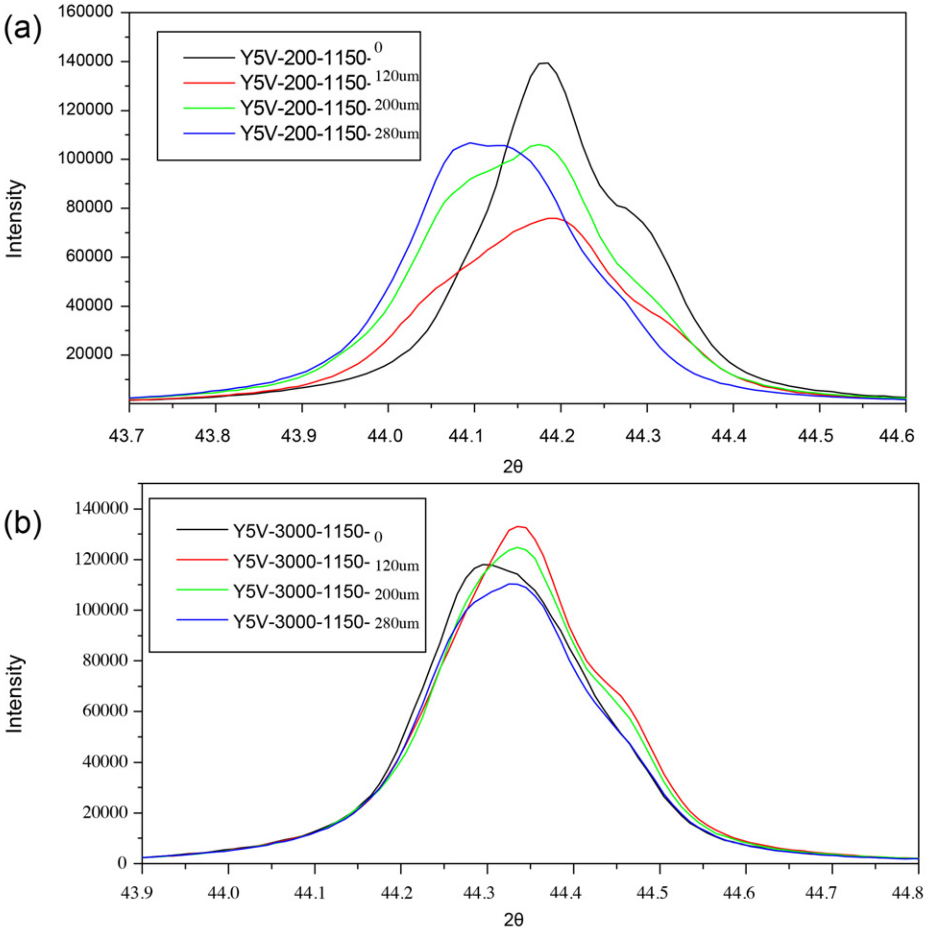

Fig. 6. (a) and (b) Thickness of the constraining layer dependence from X-ray profiles at the lapped surface in the center of MLCCs fired by constrained sintering with a slow heating rate (200 °C/H) and a high heating rate (3000 °C/H).

stresses in the three constituents of the composite structure, as one material was constrained from sintering by the others. The resulting chamber during the co-firing process can be explained by the development of these stresses.[12]

X-ray profiles of (Ba,Ca)(Ti,Zr)O_3-based MLCCs with constraining layers of different thickness were compared in (0 0 2) and (2 0 0). Residual stresses on the surface of the MLCCs were estimated by XRD analysis. The $\sin^2\theta$ XRD measurement results, in Fig. 6(a) and (b), show that the thickness of the constraining layer dependence of X-ray profiles at the lapped surface in the center of MLCCs and the residual stresses in the length direction were analyzed when the MLCCs were fired by constrained sintering with heating rates of 200 °C/H and 3000 °C/H, respectively. It was confirmed that compressive stress existed on the surface of the BCTZ-based MLCCs, and that the compressive residual stress increased with the increasing number of constraining layers, as shown in Fig. 7. The crystal structure is tetragonal and the peaks of (0 0 2) and (2 0 0) are separated. It was observed that the peaks of (0 0 2) and (2 0 0) shifted to lower angles for constrained sintering than for free sintering with a heating rate of 200 °C/H, indicating that a bigger residual stress was exhibited in MLCCs fired by constrained sintering.[13,14] However, the peaks of (0 0 2) and (2 0 0) shifted to higher angles for constrained sintering than for free sintering

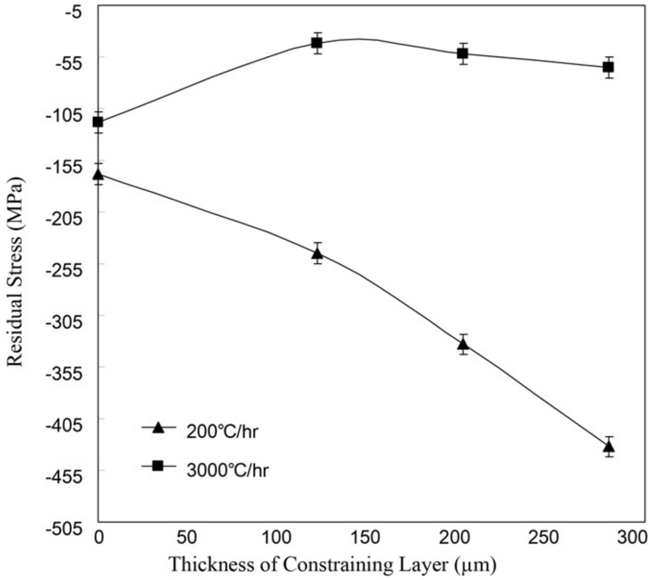

Fig. 7. Residual stress of MLCCs in the length direction fired with various heating rates as a function of the thickness of the constraining layer.

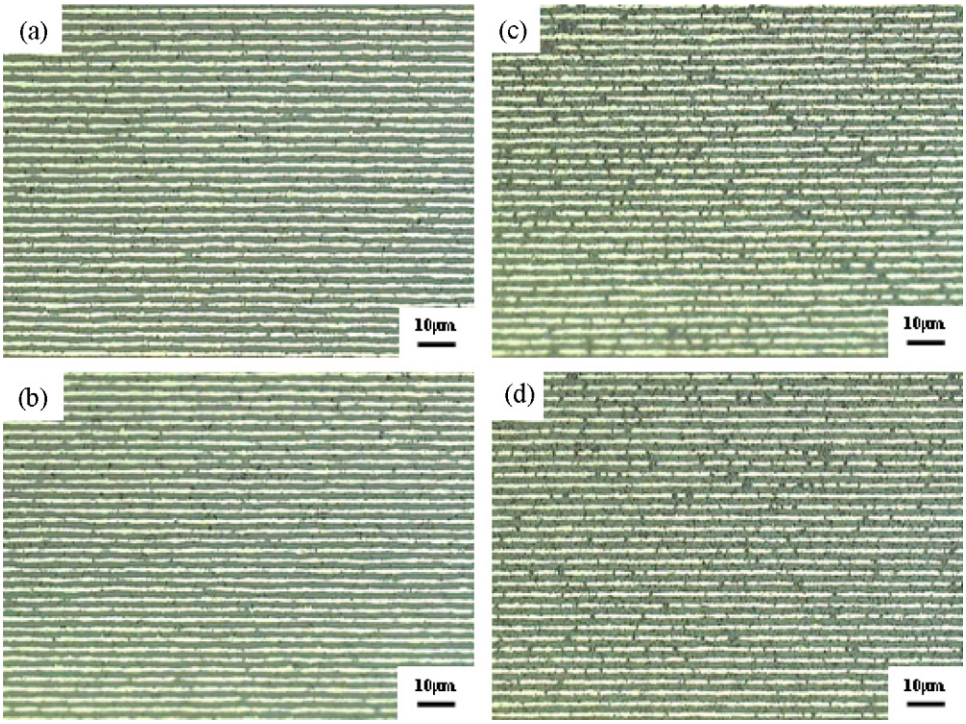

Fig. 8. (a) and (b) Optical microscopy microstructure of MLCCs fired at 1050 °C for 2 h by free sintering with heating rates of 200 °C/H and 3000 °C/H, respectively. (c) and (d) Optical microscopy microstructure of MLCCs fired at 1050 °C for 2 h by constrained sintering at heating rates of 200 °C/H and 3000 °C/H, respectively.

with a heating rate of 3000 °C/H, indicating that a smaller residual stress was exhibited in MLCCs fired by constrained sintering. To explain the discrepancy of the effect of constrained sintering with various heating rates on the residual stress in MLCCs, the chamber development during the co-firing of MLCCs was explored.

For free sintering, the residual stress of an MLCC comes mainly from the chamber development, which is attributed to the mismatch between the inner electrode and the ceramic dielectric due to their different onset temperature, densification rate and densification strain. When ceramic and electrode were co-fired by free sintering, the electrode with the lower onset temperature shrank early, so that the chamber was formed. Under the free sintering condition, the MLCC samples started flat, and then cambered towards the Ni electrode side because the densification of the Ni electrode occurred more rapidly than that of BCTZ at a temperature below the onset temperature of the BCTZ dielectric. The curvation decreased when the firing temperature climbed and became flat again, and finally cambered downward as the sintering temperature increased.[15]

On the other hand, for constrained sintering, the residual stress of MLCCs resulted not only from the chamber development, but also from the generation of friction force due to the mismatch between the ceramic dielectric as the constrained layer and the constraining layer.[16] Under the low heating rate of 200 °C/H, the chamber was first formed due to the mismatch between the electrode and ceramic dielectric, and then the friction force was generated due to the mismatch between the ceramic dielectric as the constrained layer and constraining layer. Therefore, the residual stress of MLCCs fired by free sintering was always lower than that by constrained sintering at a low heating rate of 200 °C/H. The residual stress of MLCCs fired by constrained sintering as a sum is shown in Eq. (3):

$$\sigma_{\mathrm{L}} = \sigma_{\mathrm{L(e\text{-}d)}} + \sigma_{\mathrm{L(d\text{-}c)}} \tag{3}$$

where

$$\sigma_{\mathrm{L(e\text{-}d)}} = \left(\frac{1}{1+m_1 n_1}\right)\eta_{\mathrm{eL}}\Delta\dot{\varepsilon}_{1\mathrm{L}} \tag{4}$$

where m_1 is the layer thickness ratio between the Ni electrode and BCTZ dielectric ($m_1 = h_e/h_d$), n_1 is the viscosity ratio between the Ni electrode and BCTZ dielectric layers ($n_1 = \eta_{\mathrm{eL}}/\eta_{\mathrm{dL}}$) at a low heating rate (200 °C/H) and $\Delta\dot{\varepsilon}_{1\mathrm{L}}$ is the mismatch of the densification rates between the Ni electrode and BCTZ dielectric. Obviously, the elastic stresses, $\sigma_{\mathrm{L(e\text{-}d)}}$, generated in the Ni electrode layers mainly depended on the Ni electrode viscosity, as well as on the mismatch of densification kinetics between the adjacent dielectric and electrode layers.where

$$\sigma_{\mathrm{L(d\text{-}c)}} = \left(\frac{1}{1+m_2 n_2}\right)\eta_{\mathrm{dL}}\Delta\dot{\varepsilon}_{2\mathrm{L}} \tag{5}$$

where m_2 is the layer thickness ratio between the BCTZ dielectric and BT constraining layers ($m_2 = h_d/h_c$), n_2 is the viscosity ratio between the BCTZ dielectric and BT constraining layers ($n_2 = \eta_{\mathrm{dL}}/\eta_{\mathrm{cLc}}$) at a low heating rate (200 °C/H) and $\Delta\dot{\varepsilon}_{2\mathrm{L}}$ is the mismatch of the densification rates between the BCTZ dielectric and BT constraining layers. The elastic stresses, $\sigma_{\mathrm{L(d\text{-}c)}}$, generated in the BCTZ dielectric layers were closely related to BCTZ dielectric viscosity, the layer thickness ratio between the BCTZ dielectric and BT constraining layers, and the mismatch of densification kinetics between the BCTZ dielectric and BT constraining layers.

Thus,

$$\sigma_{\mathrm{L}} = \left(\frac{1}{1+m_1 n_1}\right)\eta_{\mathrm{eL}}\Delta\dot{\varepsilon}_{1\mathrm{L}} + \left(\frac{1}{1+m_2 n_2}\right)\eta_{\mathrm{dL}}\Delta\dot{\varepsilon}_{2\mathrm{L}} \qquad (6)$$

As the thickness of the constraining layer increased, m_2 decreased, leading to an increase in the total elastic stress (σ_{L}). As a result, the measurement of residual stress of MLCCs fired by constrained sintering at a low heating rate increased with the increasing thickness of the constraining layer.[17]

When MLCCs were fired at a high heating rate instead of a low heating rate, the chamber development was minimized as the mismatch between the electrode and the ceramic dielectric was reduced by eliminating the difference in the onset densification temperature.[18] We expected that the development of camber would be minimized and the temperature of camber formation would be delayed as MLCC samples were fired by constrained sintering instead of free sintering at a high heating rate.

In addition, the chamber development between the electrode and the ceramic dielectric, as well as the generated friction force between the ceramic dielectric and the constraining layer, occurred simultaneously due to a high heating rate. Since the chamber development and the generation of friction force were proceeding almost in parallel, the friction force not only suppressed the shrinkage rate in the *x*, *y* directions of the ceramic dielectric, but also suppressed the shrinkage rate in the *x*, *y* directions of the electrode. The interaction between the chamber development and the generation of friction force which would lead to the chamber development between the electrode and ceramic dielectric was further minimized. Therefore, a sintering mismatch stress, σ_{H}, which resulted from a diminution of the mismatch of densification rate between Ni and BCTZ ($\sigma_{\text{e-d}}$) and the mismatch of densification between BCTZ and BT ($\sigma_{\text{d-c}}$) as the constraining layer can be described by:

$$\sigma_{\mathrm{H}} = \sigma_{\mathrm{H(e\text{-}d)}} - \sigma_{\mathrm{H(d\text{-}c)}} \qquad (7)$$

where

$$\sigma_{\mathrm{H(e\text{-}d)}} = \left(\frac{1}{1+m_1 n_3}\right)\eta_{\mathrm{eH}}\,\dot{\varepsilon}_{1\mathrm{H}} \qquad (8)$$

where n_3 is the viscosity ratio between the Ni electrode and BCTZ dielectric layers ($n_3 = \eta_{\mathrm{eH}}/\eta_{\mathrm{dH}}$) at a high heating rate (3000 °C/H).where

$$\sigma_{\mathrm{H(d\text{-}c)}} = \left(\frac{1}{1+m_2 n_4}\right)\eta_{\mathrm{dH}}\Delta\,\dot{\varepsilon}_{2\mathrm{H}} \qquad (9)$$

n_4 is the viscosity ratio between the BCTZ dielectric and BT constraining layers ($n_4 = \eta_{\mathrm{dH}}/\eta_{\mathrm{cLH}}$) at a high heating rate (3000 °C/H).

Thus,

$$\sigma_{\mathrm{H}} = \left(\frac{1}{1+m_1 n_3}\right)\eta_{\mathrm{eH}}\Delta\dot{\varepsilon}_{1\mathrm{H}} - \left(\frac{1}{1+m_2 n_4}\right)\eta_{\mathrm{dH}}\Delta\dot{\varepsilon}_{2\mathrm{H}} \qquad (10)$$

The viscosity of the materials generally decreased with increases in the heating rate and temperature, so η_{eH} is smaller than η_{eL} and η_{dH} is smaller than η_{deL}. The mismatch of the densification rates between two heterostructural layers also decreased with an increase in heating rate due to the elimination of the mismatch of the onset densification temperature, so $\Delta\dot{\varepsilon}_{1\mathrm{H}}$ is smaller than $\Delta\dot{\varepsilon}_{1\mathrm{L}}$ and $\Delta\dot{\varepsilon}_{2\mathrm{H}}$ is smaller than $\Delta\dot{\varepsilon}_{2\mathrm{L}}$. According to these results, under free sintering, the elastic stress level in MLCCs should be reduced with a high heating rate; in other words, $\sigma_{\mathrm{H(e\text{-}d)}}$ is smaller than $\sigma_{\mathrm{L(e\text{-}d)}}$, which is in agreement with the measurement of residual stress by XRD shown in Fig. 7.

The elastic stress, σ_{H}, in MLCCs fired by constrained sintering at a high heating rate of 3000 °C/H was also smaller than that of σ_{L} at a low heating rate of 200 °C/H. When MLCCs were fired by constrained sintering with a low heating rate, the two mismatch reactions of the Ni-electrode-BCTZ dielectric and BCTZ dielectric-BT constraining layer were sequential, so the total elastic stress was a sum of the two elastic stresses. In contrast, when MLCCs were fired by constrained sintering with a high heating rate, the two mismatched reactions of the Ni-electrode-BCTZ dielectric and BCTZ dielectric-BT constraining layer were in parallel, so the total elastic stress was a subtraction of two elastic stresses. This result was consistent with the measurement of the residual stress of MLCCs fired by constrained sintering at different heating rates.

3.3. Inner electrode continuity

Fig. 8(a) and (b), respectively, shows the continuity of the inner electrode of BCTZ-based MLCCs fired by free sintering at 1050 °C for 2 h at heating rates of 200 °C/H and 3000 °C/H. Fig. 8(c) and (d), respectively, shows the continuity of the inner electrode of BCTZ-based MLCCs fired by constrained sintering at 1050 °C for 2 h at heating rates of 200 °C/H and 3000 °C/H. Figs. 9 and 10 are same as Fig. 8, but the top sintering temperatures were 1100 and 1150 °C, instead of 1050 °C. The continuity of the Ni electrodes of MLCCs fired at 1150 °C by free sintering at heating rates of 200 °C/H and 3000 °C/H were, respectively, 80.3% and 94.9%. On the other hand, the continuity of the Ni electrodes of MLCCs fired at 1150 °C by constrained sintering at heating rates of 200 °C/H and 3000 °C/H were 96% and 98%, respectively. The inner electrode became more discontinuous for the Ni-based BCTZ dielectric fired by free sintering at a slow heating rate of 200 °C/H; however, others showed a much higher level of electrode continuity. Obviously, the heating rate and the constrained sintering both affected the stability of the inner electrodes. Fig. 11 quantifies the continuity of the inner electrodes of the MLCC samples held at 950, 1050, 1100 and 1150 °C at the top temperature for 2 h. For the Ni-based BCTZ dielectric fired by free sintering with a slow heating rate of 200 °C/H, poor electrode continuity was observed within the temperature range of 1050–1100 °C. It was observed that in the temperature range of 1050–1150 °C, the Ni-electrode continuity improved with an increase in the heating rate. However, a strong nonlinear relationship between Ni-electrode continuity and the top sintering temperature was observed. This result was consistent with previous studies by Randall et al.[19] In our materials system, the onset densification temperature of the Ni electrode, 800–850 °C, was much lower than that of the BCTZ dielectric (1050–1100 °C),

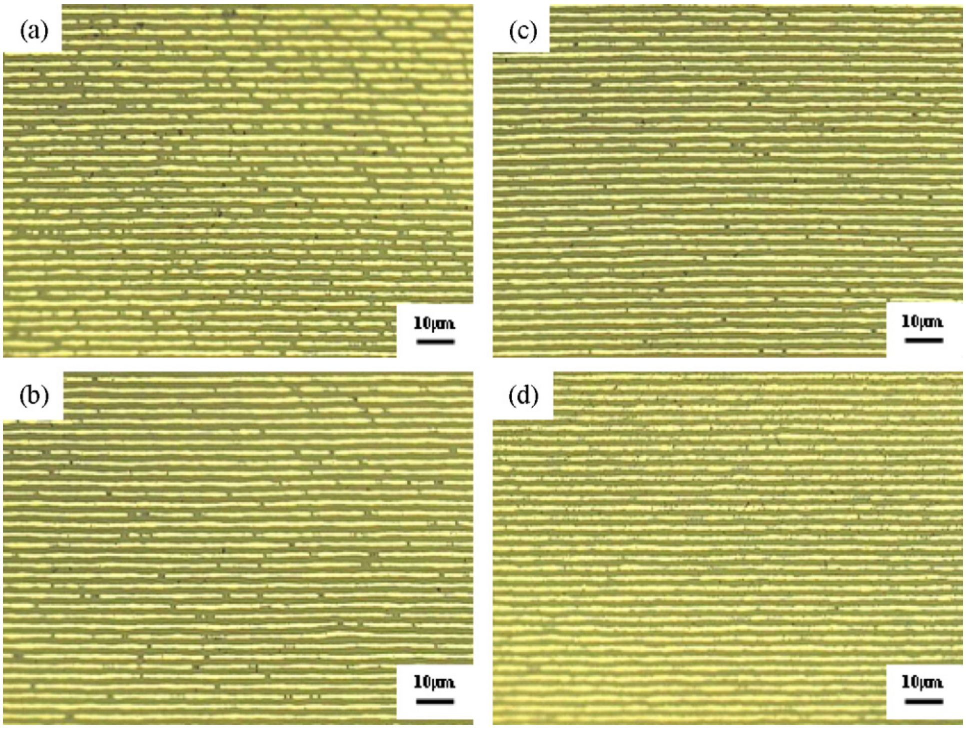

Fig. 9. (a) and (b) Optical microscopy microstructure of MLCCs fired at 1100 °C for 2 h by free sintering with heating rates of 200 °C/H and 3000 °C/H, respectively. (c) and (d) Optical microscopy microstructure of MLCCs fired at 1100 °C for 2 h by constrained sintering with heating rates of 200 °C/H and 3000 °C/H, respectively.

so an initial tensile stress in the Ni electrode was changed into a compressive stress at temperatures higher than 1050–1100 °C where the continuity of the inner electrode reverse occurred. The inner electrode continuity was greatly improved when samples were fired at a high heating rate instead of a slow heating rate. The formation of a low melting (Ni,Ba,Ti) interfacial liquid alloy, which could have resulted in poor inner electrode continuity, was strongly suppressed by the high heating rate, and the

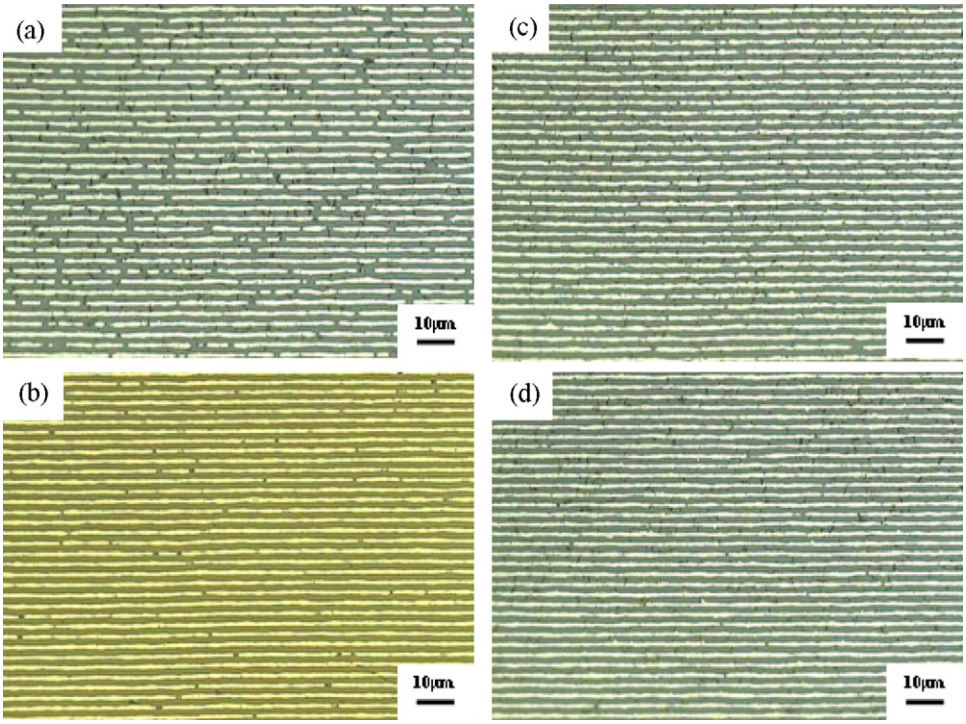

Fig. 10. (a) and (b) Optical microscopy microstructure of MLCCs fired at 1150 °C for 2 h by free sintering with heating rates of 200 °C/H and 3000 °C/H, respectively. (c) and (d) Optical microscopy microstructure of MLCCs fired at 1150 °C for 2 h by constrained sintering with heating rates of 200 °C/H and 3000 °C/H, respectively.

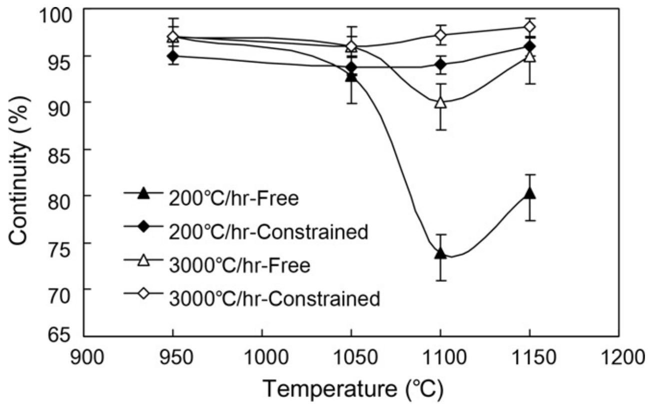

Fig. 11. Ni continuity of MLCCs fired by free sintering or by constrained sintering with heating rates of 200 °C/H and 3000 °C/H as a function of the sintering temperature.

quantity of formation of low melting point interfacial (Ni,Ba,Ti) alloy decreased with the increase in heating rate.[20] This was a kinetics approach based on the control of the interfacial alloy layer formation kinetics using a fast heating rate profile. However, there was a paradox in the observed experimental data. As the BCTZ-based MLCCs were fired by constrained sintering, the heating rate did not seem to be a key factor affecting the continuity of the Ni electrodes; all BCTZ-based MLCCs fired by constrained sintering showed very high continuity of inner electrodes (>95%), as shown in Fig. 12. This behavior could be understood when we considered that the role of the interfacial alloy layer and the densification of layer composites fired by constrained sintering was usually accompanied with elastic stress formation. We could make a reasonable assumption that the formation of a low melting point interfacial (Ni,Ba,Ti) alloy could be strongly suppressed since a compressive stress was introduced by the constrained sintering to reduce the catalytic activity of the Ni electrode. This was a thermodynamic approach to suppress the formation of a low melting point interfacial (Ni,Ba,Ti) alloy by the constrained sintering.

Obviously, not only the heating rate, but also the presence of compressive stress affected the formation of a low melting point interfacial (Ni,Ba,Ti) alloy and the stability of the inner electrode. Therefore, even when the heating rate was slow, the inner electrode continuity of the multilayer ceramic capacitor fired by constrained sintering was still very high. As noted, the electrode continuity of MLCCs fired by constrained sintering with a high heating rate of 3000 °C/H was higher than with a slow heating rate of 200 °C/H in the temperature range of 950–1150 °C. Under constrained sintering, there were two factors (kinetic heating rate and thermodynamic compressive stress) which affected the formation of low melting point interfacial (Ni,Ba,Ti) alloy. Only the thermodynamic factor stabilized the inner electrode continuity when MLCCs were fired by constrained sintering with a slow heating rate. On the other hand, the kinetic and the thermodynamic factors simultaneously stabilized the electrode continuity when MLCCs were fired by constrained sintering with a high heating rate.

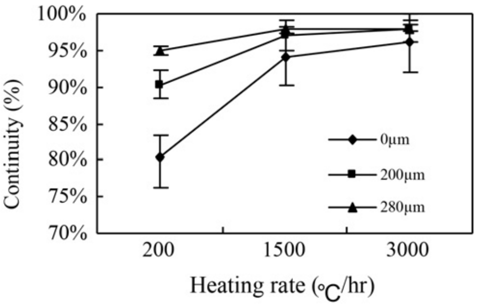

Fig. 12. Ni continuity of MLCCs fired at 1150 °C for 2 h by free sintering or by constrained sintering as a function of the heating rate.

Fig. 13(a)–(d), respectively, shows the microstructure of the inner electrode continuity for four kinds of MLCC samples. Clearly, the inner electrode of MLCCs fired by free sintering with a slow heating rate was not only discontinuous, but also wavy and distorted with large elongated pores. The average thickness of the Ni electrode was 1.36 ± 0.52 μm. When the heating rate was increased from 200 °C/H to 3000 °C/H, the Ni electrodes were essentially uniform, with few defects and an average thickness of 1.31 ± 0.15 μm.

On the other hand, for MLCCs fired by constrained sintering with a low heating rate of 200 °C/H, the Ni electrodes were again almost uniform and with few defects; the average thickness of the Ni electrode was 0.98 ± 0.15 μm, which was even thinner than for those fired by free sintering. When the heating rate increased from 200 °C/H to 3000 °C/H, the Ni electrodes were still uniform and continuous with an average thickness of 1.04 ± 0.05 μm. Although applying the high heating rate and the constrained sintering techniques both greatly improved the continuity of the Ni electrode, the thickness of the Ni electrodes of MLCCs fired by constrained sintering was much thinner than for those fired by free sintering with a fast heating rate. It was believed that the presence of in-plane tensile stress from the friction by constrained sintering not only suppressed the formation of the (Ni,Ba,Ti) alloy, but also suppressed the shrinkage of the Ni electrode in the *x*–*y* plane, which led to a high shrinkage rate in the *z* direction and a thinner Ni inner electrode.

3.4. Microstructure of BCTZ-based MLCC fired by free and constrained sintering

Fig. 14(a) and (b), respectively, shows the microstructure of BCTZ-based MLCCs fired at 1150 °C for 2 h by free sintering with heating rates of 200 and 3000 °C/H. Clearly, the grain size of MLCCs fired by free sintering at a 200 °C/H heating rate was bigger and inhomogeneous; the average grain size was 4.4 ± 0.35 μm. When the heating rate was increased from 200 °C/H to 3000 °C/H, the distribution of the grain size was more uniform and the average grain size was 3.4 ± 0.12 μm.

Fig. 14(c) and (d) shows the microstructures of BCTZ-based MLCCs fired at 1150 °C for 2 h by constrained sintering with heating rates of 200 and 3000 °C/H, respectively. Obviously, when MLCCs were fired by constrained sintering instead of free sintering at a heating rate of 200 °C/H, the grain size was very fine and the average grain size was 1.13 ± 0.11 μm, which was much smaller than for firing by free sintering. When the heating rate increased from 200 °C/H to 3000 °C/H, the distribution of

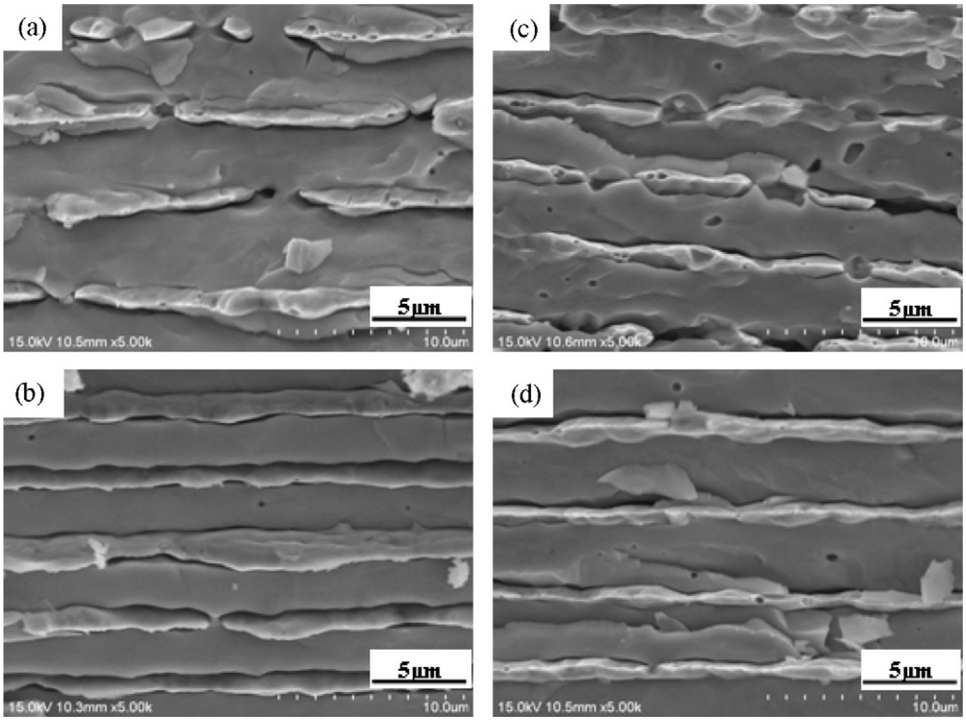

Fig. 13. (a) and (b) Scanning electronic microscopy microstructure of Ni electrodes of MLCCs fired by free sintering at 1150 °C for 2 h with heating rates of 200 °C/H and 3000 °C/H. (c) and (d) Scanning electronic microscopy microstructure of Ni electrodes of MLCCs fired by constrained sintering at 1150 °C for 2 h with heating rates of 200 °C/H and 3000 °C/H, respectively.

grain size was very fine and uniform, and the average grain size was 1.51 ± 0.04 μm. Similar to the effect of the heating rate and constrained sintering on the inner electrode, both the heating rate and the constrained sintering affected the average grain size and its distribution. Fig. 15 quantifies the grain size of MLCCs held at 1050, 1100 and 1150 °C at the top temperature for 2 h. For BCTZ-based MLCCs fired by free sintering at various heating rates, there was basically no significant difference in grain size,

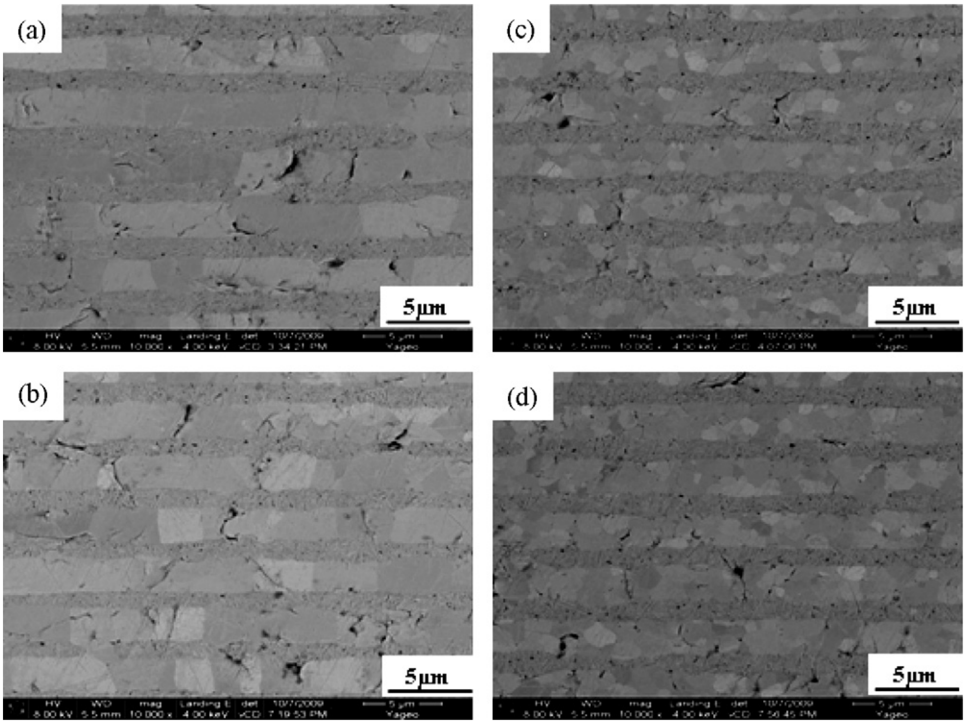

Fig. 14. (a) and (b) Scanning electronic microscopy microstructure of grain size of MLCCs fired by free sintering at 1150 °C for 2 h with heating rates of 200 °C/H and 3000 °C/H, respectively. (c) and (d) Scanning electronic microscopy microstructure of grain size of MLCCs fired by free sintering at 1150 °C for 2 h with heating rates of 200 °C/H and 3000 °C/H, respectively.

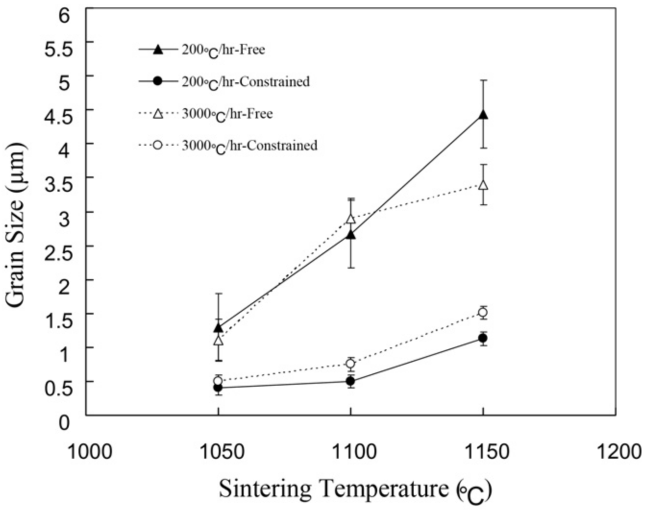

Fig. 15. Grain size of MLCC fired by free sintering or by constrained sintering with heating rates of 200 °C/H and 3000 °C/H as a function of the sintering temperature.

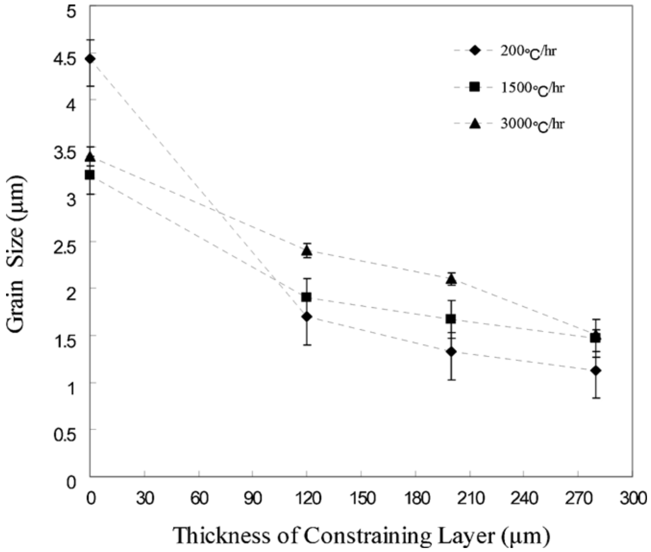

Fig. 16. Grain size of MLCCs fired at 1150 °C for 2 h by free sintering or by constrained sintering as a function of the heating rate.

but the distribution of grain size was uniform at a 3000 °C/H heating rate. It appeared that the heating rate was not a key factor in determining grain-size growth for MLCCs fired by free sintering; however, the effect of the high heating rate was valid and improved the homogeneity of grain size.[21] In comparison with MLCCs fired by free sintering, as expected, the grain size of MLCCs fired by constrained was remarkably inhibited. However, in contrast to BCTZ-based MLCCs fired by free sintering, the heating rate played an important role in determining the grain size of BCTZ-based MLCCs fired by constrained sintering, and grain size increased with an increasing heating rate.

According to the above results, we concluded that the average grain size of BCTZ-based MLCCs was significantly reduced by constrained sintering instead of free sintering, and that the homogeneity of grain size was significantly improved by rapid heating sintering instead of slow heating sintering. Constrained sintering introduced a friction force between the BCTZ-based MLCCs, and the BT constraining layer (σ_{dc}) suppressed the in-plane shrinkage. In-plane tensile stress resulting from constrained sintering in the x–y plane of the multilayer device modified the densification rate of the dielectric materials; thus, constrained sintering inhibited the rate of grain growth for each grain and the variation in grain size. The rapid heating sintering minimized the mismatch of heterostructure and improved the distribution of dopants inside the dielectric grain,[22] indicating that the homogeneity of the microstructure of the BCTZ-based MLCCs fired by rapid heating sintering was remarkably improved under either free sintering or constrained sintering.

Fig. 16 shows the effect of the thickness of the constraining layer on the grain size of MLCCs fired by constrained sintering with various heating rates. As the thickness of the constraining layer increased, the grain size decreased. As previously mentioned, in-plane tensile stress played an important role in determining grain size growth, and the degree of in-plane tensile stress was closely related to the heating rate and the thickness of the constraining layer during co-firing by constrained sintering. The in-plane tensile stress increased with the increasing thickness of the constraining layer; thus, the grain size of the BCTZ dielectric fired by constrained sintering decreased with the increasing thickness of the constraining layer.[23] However, there was a significant discrepancy in the effect of the thickness of the constraining layer on the grain size between the low and high heating rates. At the high heating rate, the mismatch of the onset densification temperature between the constrained and the constraining layers was greatly minimized, thus leading to a reduction of in-plane tensile stress. Therefore, the inhibition of the grain size of the BCTZ dielectric fired by constrained sintering with a high heating rate was not as strong as with a low heating rate.

4. Conclusions

The results of this study can be summarized as follows.

1. A novel sintering technique combining rapid heating and constrained sintering was successfully developed for firing MLCCs with Ni inner electrodes. Compared to the traditional free sintering, the microstructures of MLCCs fired by the novel sintering technique were remarkably improved, so that the stability of the electrode continuity was very high over a wide temperature range regardless of the heating rate, and the grain size was fine and uniform.
2. MLCCs fired by the novel sintering technique could be described by a viscous flow model. Controlling factors consisted of the heating rate, the thickness ratio and the densification rate ratio of the constrained layers to the constraining layers. A sintering mismatch between the constrained and the constraining layers, which was reflected in the elastic stress of MLCCs after sintering, increased with a decrease in the heating rate and an increase in the ratio of the thickness and the densification rate of the constrained and the constraining layers. How well the elastic stress was controlled was a

vital factor in the successful application of the novel sintering technique for firing multilayer ceramic capacitors.

Acknowledgement

The authors gratefully acknowledge the financial support from R.O.C. Ministry of Economic Affairs under contract No. 98-EC-17-A-17-S1-107.

References

1. Lee WH, Chen WT, Hu CL, Lee YC, Lin SP, Su CY. Characterization of ZnO-based multilayer varistor sintered by hot-press sintering. *Jpn J Appl Phys* 2006;**45**:2689–94.
2. Lin YC, Jean JH. Constrained densification kinetics of alumina/borosilicate glass + alumina/alumina sandwich structure. *J Am Ceram Soc* 2002;**85**(1):150–4.
3. Liao CH, Jean JH, Hung YY. Self-constrained sintering of a multilayer low temperature cofired glass-ceramics/alumina laminate. *J Am Ceram Soc* 2008;**91**(2):648–51.
4. Lee WH, Su CY. Improvement in the temperature stability of a $BaTiO_3$-based multilayer ceramic capacitor by constrained sintering. *J Am Ceram Soc* 2007;**90**(10):3345–8.
5. Lee WH, Chen WT, Su CY. Attaining a homogeneous microstructure of a ZnO-based multilayer varistor by constrained sintering. *J Am Ceram Soc* 2007;**90**(10):3296–8.
6. Harmer M, Roberts EW, Brook RJ. Rapid sintering of pure and doped alpha-Al_2O_3. *Trans J Br Ceram Soc* 1979;**78**(1):22–5.
7. Lu GQ, Sutterlin RC, Gupta TK. effect of mismatched sintering kinetics on chamber in a low temperature cofired ceramic package. *J Am Ceram Soc* 1993;**76**(8):1907–14.
8. Chu MY, Rahaman MN, Dejonghe LC, Brook RJ. Effect of heating rate on sintering and coarsening. *J Am Ceram Soc* 1991;**74**(6):1217–25.
9. Lee WH, Tseng TY, Hennings DFK. Effects of calcination temperature and *A*/*B* ratio on the dielectric properties of $(Ba,Ca)(Ti,Zr,Mn)O_3$ for multilayer ceramic capacitors with nickel electrodes. *J Am Ceram Soc* 2000;**83**(6):1402–6.
10. Saito K, Chazono H. Stress and electrical field responses of X5R type multilayer ceramic capacitor with Ni internal electrode. *Jpn J Appl Phys* 2003;**42**:6045–9.
11. Jean JH, Chang CR. Cofiring kinetics and mechanisms of an Ag-metallized ceramic-filled glass electronic package. *J Am Ceram Soc* 1997;**80**(12):3084–92.
12. Tzeng SY, Jean JH. Stress development during constrained sintering of alumina/glass/alumina sandwich structure. *J Am Ceram Soc* 2002;**85**(2):335–40.
13. Nakano Y, Nomura T, Takenaka T. Residual stress of multilayer ceramic capacitor with Ni-electrodes (Ni-MLCCs). *Jpn J Appl Phys* 2003;**42**:6041–4.
14. Nakano Y, Nomura T, Takenaka T. Number of dielectric layers dependence of dielectric properties and residual stress of multilayer ceramic capacitor with Ni electrodes. *Jpn J Appl Phys* 2003;**42**:6041–4.
15. Jean JH, Chang CR, Chen ZC. Effect of densification mismatch on chamber development during cofiring of nickel-based multilayer ceramic capacitor. *J Am Ceram Soc* 1997;**80**(8):2401–6.
16. Hsu RT, Jean JH. Key factor controlling camber behavior during the cofiring of bi-layer ceramic dielectric laminates. *J Am Ceram Soc* 2005;**88**(9):2429–34.
17. Yang G, Yue Z, Sun T, Jiang W, Li X, Li L. Evaluation of residual stress in a multilayer ceramic capacitor and its effect on dielectric behavior under applied dc bias field. *J Am Ceram Soc* 2008;**91**(3):887–92.
18. Cai PZ, Green DJ, Messing GL. Constrained densification of alumina/zirconia hybrid laminates. 2. Viscoelstic stress computation. *J Am Ceram Soc* 1997;**80**(8):1940–8.
19. Polotai AV, Jeong TH, Yang GY, Dickey EC, Randall CA, Pinceloup P, et al. Effect of Cr addition on the microstructure stability of Ni electrodes in ultra-thin $BaTiO_3$ multilayer capacitor. *J Electroceram* 2007;**18**:261–8.
20. Polotai AV, Yang GY, Dickey EC, Randall CA. Utilization of multiple-stage sintering to control Ni electrode continuity in ultrathin Ni–$BaTiO_3$ multilayer capacitor. *J Am Ceram Soc* 2007;**90**(12):3811–7.
21. Chazono H, Kishi H. DC-electrical degradation of the BT-based materials for multilayer ceramic capacitor with Ni internal electrode: impedance analysis and microstructure. *Jpn J Appl Phys Part I – Regular Pap Short Notes Rev Pap* 2001;**40**(9B):5624–9.
22. Polotai AV, Fujii I, Shay DP, Yang GY, Dickey EC, Randall CA. Effect of heating rates during sintering on the electrical properties of ultra-thin Ni–$BaTiO_3$ multilayer ceramic capacitor. *J Am Ceram Soc* 2008;**91**(8):2540–4.
23. Cai PZ, Green DJ, Messing GL. Constrained densification of alumina/zirconia hybrid laminates. 1. Experimental observation of processing defects. *J Am Ceram Soc* 1997;**80**(8):1929–39.